Structural mechanism of the active bicarbonate transporter from cyanobacteria

Chengcheng Wang[1,3], Bo Sun[2], Xue Zhang[1,3], Xiaowei Huang[1,3], Minhua Zhang[1], Hui Guo[1], Xin Chen[1,3], Fang Huang[4], Taiyu Chen[4], Hualing Mi[1], Fang Yu[5], Lu-Ning Liu[4], Peng Zhang[1].

[1] National Key Laboratory of Plant Molecular Genetics, CAS Center for Excellence in Molecular Plant Sciences, Institute of Plant Physiology and Ecology, Shanghai Institutes for Biological Sciences, Chinese Academy of Sciences, Shanghai 200032, China

[2] Shanghai Institute of Applied Physics, Chinese Academy of Sciences, Shanghai 201800, China

[3] University of Chinese Academy of Sciences, Beijing 100039, China

[4] Institute of Integrative Biology, University of Liverpool, Liverpool L69 7ZB, United Kingdom.

[5] Department of Biology, College of Life and Environmental Sciences, Shanghai Normal University, Shanghai 200234, China.

[*] **Correspondence**: Peng Zhang (pengzhang01@sibs.ac.cn); Tel: +86-21-5492-4219

Running title: Structure of cyanobacterial bicarbonate transporter BicA

Keywords: bicarbonate transporter; CO_2-concentrating mechanisms; photosynthesis; carbon fixation; solute carrier (SLC); STAS domain; transport mechanism

Abstract

Bicarbonate transporter plays essential roles in pH homeostasis of mammals and photosynthesis of aquatic photoautotrophs. A number of bicarbonate transporters have been characterized, among which BicA is a low-affinity, high-flux SLC26 family bicarbonate transporter involved in cyanobacterial CO_2-concentrating mechanisms to accumulate CO_2 and improve photosynthetic carbon fixation. Here, we report the three-dimensional structure of BicA from *Synechocystis sp.* PCC6803. Crystal structures of the transmembrane domain ($BicA^{TM}$) and the cytoplasmic STAS domain ($BicA^{STAS}$) of BicA were solved respectively. $BicA^{TM}$ is captured in an inward-facing HCO_3^--bound conformation and adopts a "7+7" fold monomer. HCO_3^- binds in a cytoplasm-facing hydrophilic pocket within the membrane. $BicA^{STAS}$ is assembled as a compact homodimer structure and is required for BicA dimerization. The dimeric structure of BicA was further characterized by cryo-electron microscopy on the full-length BicA and physiological analysis, and may represent the physiological unit of SLC26 family transporters. Comparing the $BicA^{TM}$ structure with the outward-facing transmembrane domain structures of other bicarbonate transporters suggests an elevator transport mechanism applicable for the SLC26/4-family sodium-dependent bicarbonate transporters. This study advances our knowledge of the structures and functions of cyanobacterial bicarbonate transporters, and will inform strategies for bioengineering functional BicA in heterologous organisms to boost CO_2 assimilation.

Introduction

Carbon dioxide exists in chemical equilibrium with bicarbonate ubiquitously in biological systems. The conversion of carbon dioxide to bicarbonate facilitates transport of carbon dioxide into the cell, and is pivotal for maintaining pH homeostasis[1]. In mammals, carbon dioxide is the principal metabolite of respiration occurring in the mitochondria. In plants and aquatic photoautotrophs, carbon dioxide and bicarbonate serve as the major carbon sources essential for photosynthesis and carbohydrate production[2-4]. Unlike carbon dioxide that can diffuse freely across biological membranes, bicarbonate is poorly permeable to lipid bilayers and requires membrane-spanned bicarbonate transporters to actively pass through membranes.

In cyanobacteria, bicarbonate transporters located in the plasma membranes cooperate with the CO_2-uptake complexes[5-8] and the CO_2-fixing organelles − carboxysomes in the cytoplasm[9-12] to form effective CO_2-concentrating mechanisms (CCM), which substantially accumulate CO_2 to facilitate the carboxylation of ribulose-1, 5-bisphosphate carboxylase/oxygenase (Rubisco), and thereby enhance CO_2 fixation[13,14]. Three bicarbonate transporters BCT1, SbtA, and BicA have been identified in cyanobacteria[13]. BicA functions as a low-affinity, high-flux, Na^+-dependent HCO_3^- transporter widely distributed among cyanobacterial species[7,15] and has been considered as a promising target to be introduced into plant chloroplasts to improve photosynthesis[16,17]. However, no active BicA has been heterologously expressed in the model plants Arabidopsis and tobacco[18-20], emphasizing the pressing need for detailed mechanistic understanding of the structures, activation and regulation of bicarbonate transporters.

Cyanobacterial BicA contains an N-terminal transmembrane domain ($BicA^{STAS}$) and a C-terminal STAS (sulfate transporter and anti-sigma factor antagonist) domain ($BicA^{STAS}$) [21,22], a characteristic feature of the solute carrier 26 (SLC26/SulP) family transporters in eukaryotes and prokaryotes[23]. A number of bicarbonate transporters of SLC4 and SLC26 families, including the SLC4A1–5, 7–10 and SLC26A3, 4, 6 transporters which function as Cl^-/HCO_3^- exchangers or Na^+/HCO_3^- co-transporters in humans, have been physiologically characterized[24-26]. Mutations of these bicarbonate transporters could cause severe human diseases, such as distal/proximal renal tubular acidosis (SLC4A1/SLC4A4)[27,28], intestinal chloride losing diarrhea (SLC26A3)[29,30] and congenital deafness (SLC26A4)[31,32], indicating their physiological significance and the necessity of dissecting their structures and transport mechanisms. To date, only two structures of the SLC4-family bicarbonate transporters have been resolved, including the transmembrane domains of human erythrocyte AE1 (anion exchange 1 or SLC4A1), which serves as a Cl^- dependent HCO_3^- exchanger[33], and human NBCe1 (SLC4A4), which is a Na^+-dependent HCO_3^- symporter[34]. Both structures represent the substrate-free outward-facing conformation. In a word, the inward-facing conformation structure and the substrate-binding sites of bicarbonate transporters remain elusive, although there are structures of related transporters (different substrates) reported in the inward-facing state [35,36].

In this study, crystal structures of $BicA^{TM}$ and $BicA^{STAS}$ domains of BicA from the model cyanobacterium *Synechocystis sp.* PCC6803 (Syn6803) are solved respectively, while the full-length BicA architecture is demonstrated with a Cryo-electron microscopy (Cryo-EM) model. Structural based functional analyses reveal molecular mechanisms underlying substrate specificity and transport of SLC26/SLC4 family

bicarbonate transporters.

Bicarbonate transport activity of BicA requires STAS domain

To verify the activity of BicA, we conducted functional assays on Syn6803 wild type and mutants that were depleted of CO_2-uptake systems and bicarbonate transporters, Δ4 (Δ*ndhD3*/*ndhD4*/*cmpA*/*sbtA*)[6] and Δ5 (Δ*ndhD3*/*ndhD4*/*cmpA*/*sbtA*/*bicA*)[37]. In the absence of BicA, the growth of Δ5 cells was significantly impeded in air (contain 0.038% CO_2 v/v) (**Figs. 1a and 1b**) and was impaired under 1% CO_2, compared with those of WT and Δ4 cells (**Extended Data Fig. 1a**). Likewise, HCO_3^- uptake activity of Δ5 cells was notably reduced compared with those of WT and the Δ4 mutant (**Extended Data Fig. 1b**). These results revealed the essential roles of BicA bicarbonate transporter in cyanobacterial CO_2 assimilation.

We further generated the Δ5/*psbA2::bicA* and Δ5/*psbA2::bicA*^{TM413} strains to rescue the Δ5 strain, by overexpressing the full-length BicA or the transmembrane domain of BicA (1-413 residues, BicA^{TM413}) under the *psbA2* promoter **(Fig. 1c)**. Under the air condition, the growth of Δ5/*psbA2::bicA* cells is comparable to that of Δ4 cells, whereas Δ5/*psbA2::bicA*^{TM413} cannot survive (**Fig. 1d**), revealing that the transmembrane domain of BicA alone is unable to actively transport bicarbonate and the STAS domain plays an essential role in bicarbonate transport activity of BicA.

Structure of BicA^{TM} in an inward-facing HCO_3^--bound conformation

To gain insight into the architecture of BicA, we crystallized the full-length BicA expressed and purified with high homogeneity in *Escherichia coli* (*E. coli*). However, only poor diffraction (~20Å) was achieved. After numerous efforts, we decided to

express separately the transmembrane domain containing 1-393 residues ($BicA^{TM393}$) and the STAS domain comprising 409-564 residues ($BicA^{STAS}$) for structure determination (**Extended Data Fig. 1c** and **1d**).

$BicA^{TM393}$ was crystallized using lipid cubic phase system, and the structure was determined to 2.8 Å resolution by molecular replacement using the transmembrane domain structure of SLC26Dg as a search model[35] (**Supplementary Table-1** and **Fig. 2a** and **2b**). Structure of $BicA^{TM393}$ contains 13 transmembrane segments (TMs); the 14^{th} TM is missing because of C-terminus truncation and is modelled based on the SLC26Dg structure (**Fig. 2a**). The transmembrane domain of BicA ($BicA^{TM}$) is organized into two inverted-topology repeats, TM1–7 and TM8–14 (**Fig. 2b**). This "7+7" fold exists not only in the SLC26 family of bicarbonate transporters, but also in the SLC4 (human AE1[33], human NBCe1[34], *Arabidopsis thaliana* Bor1[38]) and SLC23 (*E.coli* UraA[39,40] and *Aspergillus nidulans* UapA[36]) families of transporters, although that they share less than 10% sequence identity. A key feature of this fold is that helix α3 and helix α10 only extend halfway through the membrane, followed by random coiled-coils that crossover in the middle of the protein.

The 14 TMs of BicA can be divided into two domains, a core domain formed by TM1–4 and TM8–11 and a gate domain formed by TM5–7 and TM12–14 (**Fig. 2b**). The gate domain connects the upper half part of the core domain and forms an inverted "V" shape (**Fig. 2a**). A hydrophilic cavity facing the cytoplasm is present at the interface between the core and gate domains (**Fig. 2c**). Within the cavity, positive electron density peaks were observed, tentatively interpreted as HCO_3^- and a metal ion (**Extended Data Fig. 2c**). The former was added during crystallization and appeared

147 to be required for better diffraction. A lipid molecule, monoolein, is seen to bridge the
148 gate and core domains through extensive hydrophobic interactions (**Fig. 2c,** and
149 **Extended Data Fig. 2d**). This lipid molecule likely helps stabilize the inward-facing
150 conformation, as similar detergent molecules were also discerned in the relevant
151 position of SLC26Dg/UapA structures[35,36]. Overall, the BicA^{TM} structure we obtained
152 represents an inward-facing HCO_3^--bound conformation.
153
154 **HCO_3^- and metal ion binding site**
155 The HCO_3^- molecule and metal ion bind within a hydrophilic pocket formed by TM3,
156 TM8, TM10, and the connecting coiled-coils within the membrane (**Figs. 3a and 3b**).
157 Relatively conserved residues are responsible for the hydrophilic pocket formation
158 and coordinate HCO_3^- and the metal ion. HCO_3^- forms at least four coordinates with
159 the carbonyl group of Thr69 from the N-terminus of TM3, the carbonyl group of
160 Ala301 from the N-terminus of TM10, as well as the metal ion; The metal ion
161 pentacoordinates residues Asp258 and Thr262 from TM8, Gly300 and Thr302 from
162 TM10, as well as HCO_3^- (**Fig. 3b**). Given that BicA was previously characterized as a
163 Na^+-dependent HCO_3^- transporter [7] and similar pentacoordinates have been usually
164 seen in other sodium coupled transporters[41,42] (**Extended Data Fig. 3**), we tentatively
165 build the metal ion here as a Na^+ molecule (**Fig. 3b**). Mutations of residues Thr69,
166 Asp258, Thr262, Thr302 impeded the growth of Syn6803 cells, suggesting the
167 importance of these amino acid residues in binding with HCO_3^- and Na^+ (**Fig. 3c**).
168
169 The substrate-binding pockets with similar structural elements have been previously
170 reported in the SLC23 family of transporters UraA and UapA, coordinating different
171 substrates, uracil and xanthine, respectively[36,39,40]. Superimposition of the structures

of $BicA^{TM}$, UraA and UapA reveals that TM3 in $BicA^{TM}$ moves closer down to TM10, resulting in a smaller substrate-binding pocket than those in UraA and UapA (**Fig. 4a**). It may facilitate accommodation of the small substrate HCO_3^-. Moreover, structural comparison of $BicA^{TM}$ with the transmembrane domains of human bicarbonate transporters $AE1^{CTD}$ and $NBCe1^{CTD}$ reveals a good match of the structural elements of the substrate-binding pockets (**Fig. 4b**). Zoom-in view of the superimposed structures shows that the residues constituting the HCO_3^--binding site are also highly conserved (**Fig. 4c**).

However, AE1 was reported as a Cl^--coupled HCO_3^- transporter, whereas BicA and NBCe1 are Na^+-coupled HCO_3^- transporters. Multiple sequence alignment shows that residue Asp258 in BicA, which may be responsible for Na^+ binding, is conserved among Na^+-coupled bicarbonate transporters (SLC4A4/5/7/9) (**Fig. 4d**). A Glu residue is present at the corresponding position in the Na^+-independent SLC4 anion exchanger (AE1-3), probably responsible for proton binding[43]. Nevertheless, a short-chain aliphatic residue is present at the same position of the SLC26 family of HCO_3^-/Cl^- exchangers, indicating that the cations (Na^+ or H^+) may not be required during HCO_3^- transport process. Additionally, a highly conserved Arg residue is found at the N-terminus of TM10 in all the Cl^--coupled HCO_3^- transporters, but not in the Na^+-coupled HCO_3^- transporters (**Fig. 4d**). This arginine in AE1 (Arg730) was supposed to play an important role in HCO_3^- binding[33]. However, a corresponding residue in $BicA^{TM}$ (Gly304) is distant from the HCO_3^- binding site. We speculate that this highly-conserved Arg residue in the HCO_3^-/Cl^- transporters might be involved in Cl^- binding rather than HCO_3^- binding, which needs further verification.

STAS domain is required for the dimerization of active BicA

We also solved the crystal structure of $BicA^{STAS}$, which forms a compact homodimer (**Fig. 5a** and **Supplementary Table-1**). Each protomer contains residues 409-564 that form five β-strands and five α-helices. Two protomers are assembled as a three-layered dimer (**Fig. 5a** and **Extended Data Fig. 4a** and **4b**). The middle layer is constituted by five β-strands from each $BicA^{STAS}$ protomer, which forms the groundwork of the dimer. The middle layer is sandwiched by three helices (α2-α4, and α2'-α4') from each protomer in the bottom layer and another two helices (α1, α5, and α1', α5') from each protomer in the top layer (**Fig. 5b)**. Compared with the monomeric STAS domain of SLC26Dg which forms a globular domain, the $BicA^{STAS}$ protomer has an extra β3 and a perpendicular α2 inserted between α1 and β4 that form an extended conformation (**Extended Data Fig. 4c** and **4d**). When forming the dimer, β3 of molecule A is inserted into the interspace between β1' and β4' of molecule B, and β1 and β2 are inserted into the space between β2' and β3' to form the 10-stranded β-sheet (**Fig. 5a)**. In contrast, the STAS domain of SLC26Dg forms a heterodimer with the nanobody Nb5776 by constituting a 10-stranded β-sheet (**Extended Data Fig. 4e**)[35].

A wealth of physiological and biochemical data have demonstrated that the SLC26 family transporters function as dimers or oligomers[44-48]. We further tested the oligomeric state of BicA in solution. The molecular weight of BicA is 111 kDa, measured by size-exclusion chromatography coupled with multiple angle light scattering (SEC-MALS), about twice the calculated molecular mass of monomeric BicA (59.5 kDa) (**Fig. 5c**). This demonstrates explicitly that the full-length BicA proteins appear as homodimers. Chemical cross-linking experiment coupled with

SDS-PAGE analysis confirmed the dimerization of BicA in solution (**Extended Data Fig. 5a**). In addition, the transmembrane domain $BicA^{TM413}$ alone or STAS domain β1-β2 deletion mutant ($BicA^{del\beta1\text{-}2}$) appears mainly as a monomer in solution (**Figs. 5d, 5e** and **Extended Data Fig. 5b**), consistent with $SLC26Dg^{TM}$ (PDB code: 5IOF) [35] but distinct from the back-to-back dimer observed in the SLC4 and SLC23-family transporters[33,40]. These results imply that the STAS domain at the C-terminus is required for BicA dimerization.

To further clarify the oligomeric state of BicA and the relationship of $BicA^{TM}$ and $BicA^{STAS}$, we obtained the Cryo-EM structure of BicA in detergent solution (**Figs 6a, 6b** and **Extended Data Fig. 6**). Although the resolution gained is limited due to the relatively small size of BicA and structural flexibility, the Cryo-EM structure allow us to visualize the overall architecture of the BicA dimer and the allocations of $BicA^{TM}$ and $BicA^{STAS}$ domains. The $BicA^{TM}$ and $BicA^{STAS}$ crystal structures could fit very well to the density envelope, demonstrating that the BicA dimer is formed via the $BicA^{STAS}$ domain. This is consistent with the above crystal structures and biochemical analysis. In addition, we find that some of the human disease-related mutations of SLC26-family transporters[30,49,50] can be plotted onto the dimer interface of $BicA^{STAS}$ (**Fig. 6c** and **Extended Data Fig. 7**) and mutation of the corresponding residues in $BicA^{STAS}$ could notably impede cell growth (**Fig. 6d)**, suggesting the physiological significance of BicA dimerization.

We further examined the *in vivo* distribution of BicA using GFP tagging and live-cell confocal microscopy imaging. BicA-GFP appears to be evenly distributed in the cytoplasmic membranes of Syn6803, while deletion of the C-terminal STAS domain

results in clustering and spotty distribution of $BicA^{TM}$ in the cytoplasmic membranes (**Fig. 6e**). Fluorescence profile analysis confirmed the distinct distribution patterns of BicA and $BicA^{TM}$ in the cytoplasmic membranes of Syn6803 (**Fig. 6f**). Taken together, all the above data strongly suggest that $BicA^{STAS}$ is required for BicA dimerization, and BicA dimerization is essential not only for bicarbonate transporter activity, but also for its physiological membrane distribution.

Discussion

The cyanobacterial CCM plays a key role in enhancing photosynthetic carbon assimilation, allowing cyanobacteria to make a significant contribution to global primary productivity. Active inorganic carbon uptake performed by transporters in the cellular membranes is vital for the functional cyanobacterial CCM. In this study, we carried out thorough structural and functional analyses of BicA, a representative bicarbonate transporter of SLC26 family. Structure and structural-based analyses reveal the dimeric structure of active BicA, the probable binding site of HCO_3^-/Na^+, the molecular mechanisms of substrate selectivity and transport, and the functional mechanism of BicA in cell physiology and CO_2 assimilation. In particular, the role of the STAS domain in BicA dimer formation is elucidated. Such a mechanism might be unique for SLC26 family transporters featured with a C-terminal STAS domain.

Although many bicarbonate transporters have been characterized to be of physiological importance in different organisms, the mechanism of bicarbonate transport remain unclear. In a previous study, the human SLC4 family HCO_3^-/Na^+ transporter NBCe1 was solved in an outward-open conformation[34]. Here, the $BicA^{TM}$ structure exhibits an inward-facing HCO_3^--bound conformation (**Fig. 2**). Although

BicA and NBCe1 belong to different families of Na^+-dependent bicarbonate transporters, they share many structural features. The transmembrane domains of BicA and NBCe1 are of similar architecture named the "7+7" fold (**Fig. 7a**). Likewise, both $BicA^{TM}$ and $NBCe1^{CTD}$ contain a core domain and a gate domain, which can be independently superimposed well with each other (RMSDs of 2.5Å and 3.0Å, respectively), better than superimposing the whole structures of $BicA^{TM}$ and $NBCe1^{CTD}$ (RMSDs of 3.8Å) (**Extended Data Fig. 8a-8c**). By aligning the $BicA^{TM}$ and $NBCe1^{CTD}$ structures through the gate domain, we found that the two core domains undertake a rigid-body like movement **(Figs. 7a and 7b)**. The HCO_3^--binding site in the outward-facing NBCe1 (denoted by a red star) moves ~6Å upward compared with the inward-facing BicA, a hallmark sign of typical elevator mechanism[51] **(Fig. 7c)**. Similar results could be obtained by comparing $SLC26Dg^{TM}$ and $NBCe1^{CTD}$ structures together. This implies that BicA, NBCe1 and possibly SLC26 family transporters use the elevator mechanism for across membrane transport. A similar mechanism has been proposed for UraA and Bor1[38,40]. Hence, the elevator mechanism could be widely adopted by different transporter families varying greatly in domain composition and substrate.

Based on small-angle neutron scattering analysis, Compton *et al* reported the envelope structures of two SLC26 family transporters from *Yersinia enterocolitica* (YeSlc26A2) and *Escherichia coli* (DauA)[46,52], and proposed a dimer model of the bicarbonate transporter structure: the N-terminal TM domains form a dimer mediated by the core domains whereas the C-terminal STAS domains locate at the distal region of TM. However, this model was not supported by subsequent structural studies which suggested that membrane proteins with typical "7+7" fold structures form dimers

through the gate domains instead of the core domains of TM: the SLC4 family transporters NBCe1, AE1 and Bor1, and the SLC23 family transporters UraA and UapA all form dimers through the gate domains in structure and solution[33,34,36,38,40]. Interestingly, these dimer structures differ in the dimer interfaces, indicating distinct dimerization manners (**Extended Data Fig. 8d**). UraA/UapA forms a compact homodimer through two transmembrane helices from gate domain, while the dimerization of NBCe1, AE1 and Bor1 only involves one transmembrane helix from the gate domain and is relatively loose. In contrast, our data demonstrate explicitly that the functional BicA dimer is formed through the dimerization of the STAS domain at the C-terminus of BicA. This is strongly supported by an unpublished Cryo-EM structure of human SLC26 family transporter (personal communication) and a very recently published structure of murine SLC26A9 transporter [53]. Collectively, the BicA structure may represent a new structural model of the SLC26 family transporters that comprise an N-terminal transmembrane domain and a C-terminal STAS domain.

Currently, we have no direct evidence on the physiological role of the STAS domain in governing the transporter activity of SLC26 family transporters. Several studies have reported that the STAS domains of human SLC26 family bicarbonate transporters SLC26A3, SLC26A6 and SLC26A9 interacted with the R domain of CFTR (cystic fibrosis transmembrane conductance regulator)[54] and the STAS domain of *A. thaliana* Sultr1/2 bound with cysteine synthase[55]. These findings implied that the activity of the SLC26 family transporters might be dependent on interaction partners, as the primary sequences of STAS domains vary significantly. It was also postulated that the inactivation of BicA installed in *E. coli*, *Xenopus laevis* oocytes, and plants

was likely ascribed to the lack of BicA-specific regulatory factors during the engineering of BicA[17,20]. We speculate that the conformational dynamics of the BicA transmembrane domain during the transport process is regulated by the dimerized STAS domain; such a regulation might be dependent on binding of extra regulatory factors.

There is currently intriguing interest in engineering cyanobacterial CCM into plant chloroplasts to supercharge photosynthesis and crop yields, which include the construction of functional carboxysomes and installation of active HCO_3^- and CO_2 uptake systems. Recently, functional cyanobacterial Rubisco assembles and carboxysome-like structures have been reconstituted in *E. coli* and tobacco[56-58] – key steps towards building entire functional CCM in plant chloroplasts. Our analysis of the structure and function of BicA provides insight into the molecular mechanisms underlying the HCO_3^- cross-membrane transport process, and may inspire bioengineering of functional bicarbonate transporters in heterologous hosts, with the intent of improving photosynthesis and agricultural production.

Methods

Construction of BicA mutants. Construction of the Δ*ndhD3*/*ndhD4*/*cmpA*/*sbtA* mutant (designated Δ4)[6] and Δ*ndhD3*/*ndhD4*/*cmpA*/*sbtA*/*bicA* mutant (designated Δ5)[37] of Syn6803 have been described previously. The Δ5 strain was respectively rescued at psbA2 locus by transformation with the pPSBA2 vector containing a Erythromycin resistance (Er^R) gene and the fragment encoding for BicA or BicA mutants to produce the Δ5/*psbA2*::*bicA* or Δ5/*psbA2*::*bicA* mutant strains, which have been identified by PCR analysis (**Extended Data Fig. 9**). Generation of GFP-fusion strains was carried out as described previously[59]. GFP fusions were created by inserting the eGFP:apramycin region to the C terminus of *bicA* or $bicA^{TM}$ at their native chromosomal loci and under the control of their endogenous promoter.

Growth assay. Wild-type, Δ4, Δ5, Δ5/*psbA2*::*bicA* and Δ5/*psbA2*::*bicA* mutant cells were grown at 30 °C in BG11 medium and bubbled with either 1% CO_2 in air (v/v) or air alone (0.038% v/v CO_2). Cell growth was measured using OD730 absorbance. All experiments were repeated three times.

Cell-based bicarbonate uptake assay. Transport activity of Syn6803-BicA was characterized using a whole-cell assay of [^{14}C] bicarbonate uptake. The wild-type, Δ4 and Δ5 cells were first grown at 30 °C under BG11 medium (pH 8.0) bubbled with air plus 1% CO2 for two days, then the medium was bubbled with air alone (0.038% v/v CO_2) for four hours. The cells were diluted and aligned to a chlorophyll density of 2 μg/ml. To perform the uptake assay, 250μl of cell suspension was mixed with equal volume of BG11 medium containing 200 μM $NaH^{14}CO_3$ (PerkinElmer), 400 μM

363 $NaHCO_3$ and 30 mM NaCl. Then the HCO_3^- uptake was initiated by illuminating the
364 cells using white light (600 μE m^{-2} s^{-1}) and terminated after 30s by rapid filtration of
365 the cells onto a 0.22 μm cellulose acetate filter (Sartorius) by suction, followed by
366 immediate washing of the filter with 10ml BG11 medium. The filters were incubated
367 for 10 min in scintillation fluid before measuring radioactivity with a liquid
368 scintillation counter (LS 6500, Backman). All experiments were repeated three times.
369
370 **Gene cloning and protein purification.** The gene encoding the bicarbonate
371 transporter Syn6803-BicA was amplified by PCR from *Synechocystis sp.* PCC6803
372 genomic DNA. The gene ID and predicted molecular mass are 499176153 and
373 59.1kDa. The full-length BicA was cloned into pET28a vector. Eight truncations of
374 transmembrane domain ($BicA^{TM}$: 1-383/393/403/403/433/443/463/473), five
375 truncations of STAS domain ($BicA^{STAS}$: 403/409/414/419/424-564), and one deletion
376 ($BicA^{delβ1-2}$: residues from Asp405 to Ala421 were deleted) of BicA were respectively
377 cloned into pRSFDuet vector. A six-histidine tag was added at the N-terminus of all
378 proteins. For BicA and $BicA^{TM393}$ protein expression, plasmids were transformed into
379 *Escherichia coli* BL21 (DE3) and induced by 0.25 mM β-D-thiogalactopyranoside
380 (IPTG) at OD600 of about 1.2. After 14h at 37 °C, the cells were harvested, and
381 homogenized in buffer A (100 mM NaCl, 20 mM Tris-HCl pH8.0), and lysed using a
382 French press. Cell debris was removed by centrifugation. The supernatant was
383 collected and applied to ultracentrifugation at 150,000g for 1 h. Membrane fraction
384 was incubated with 1% (w/v) n-dodecyl-β-D-maltopyranoside (DDM; Bluepus) for 2h
385 at 4 °C. After another centrifugation step at 20,000g for 45min, the supernatant was
386 loaded onto a Ni^{2+}-NTA affinity column (Qiagen), and washed with buffer B (100
387 mM NaCl, 20 mM Tris-HCl pH 8.0 and 0.018% DDM) plus 25 mM imidazole. The

protein was eluted from the column using buffer B plus 250 mM imidazole, and was concentrated to around 10 mg/ml before further purified by gel filtration (Superdex-200, GE Healthcare) in buffer C (100 mM NaCl, 20 mM Tris-HCl pH 8.0 and 0.18% n-decyl-β-d-maltoside (DM, Anatrace). The peak fraction was collected and concentrated to 5∼10 mg/ml for crystallization.

For $BicA^{STAS}$ expression, plasmids were transformed into *E. coli* BL21 (DE3) strain. The transformed cells were grown at 37 °C and induced by 0.25 mM IPTG for 12 h at 25 °C. The cells were harvested, resuspended in buffer A (20 mM Tris-HCl pH 8.0, 100 mM NaCl) and lysed using French Press. The total lysate was centrifuged at 20,000× g for 45 min before the supernatant was loaded onto a Ni^{2+}-NTA column for purification. After competitive wash with buffer A plus 25 mM imidazole, protein sample was eluted with buffer A plus 250 mM imidazole, and further purified by gel filtration. Peak fractions were collected and concentrated for subsequent studies. For the Selenium-methionine $BicA^{STAS}$ expression, a published protocol was adopted[60].

Crystallization, data collection and structure determination. Crystallization of $BicA^{TM393}$ was carried out using both vapor diffusion method and lipid cubic phase (LCP) method. 1mM $NaHCO_3$ was added to the protein sample before crystallization. For crystallization with vapor diffusion method, protein was concentrated to 5 mg/ml. The best crystals were grown under 0.1 M KCl, 0.1 M Tris pH7.0 and 39% PEG400 (protein: reservoir volume in 1:1 ratio) at 20 °C, and were directly flash frozen in liquid nitrogen for data collection. But these crystals diffracted to around 8Å resolution which could not be further improved. For LCP crystallization, protein was concentrated to 10 mg /ml and mixed with 1.5-folds of monoolein in a coupled

syringe device to make LCP. Protein containing LCP was dispersed onto a glass plate as 50 nl bolus, and covered with 600 nl of precipitant solution using a Gryphon robot. Rod-shaped crystals were grown in precipitant solution containing 0.1M NaCl, 0.1 M Li_2SO4, 0.1 M Na-citrate, pH5.0, 30% PEG600 at 20 °C. Crystals used for data collection were directly flash-frozen in a cold nitrogen stream at 100 K. Crystallization of $BicA^{STAS}$ was carried out by sitting drop vapor diffusion method at 20 °C. The best selenium-methionine crystals were grown under a condition containing 20 mM $MgCl_2 \cdot 6H_2O$, 2 mM $CoCl_2 \cdot 6H_2O$, 50 mM HEPES, pH7.5, 2.0 M $(NH_4)_2SO_4$, 1 mM spermine. All data were collected at BL19U1 beamline and BL17U beamline at the Shanghai Synchrotron Radiation Facility (SSRF) and processed with HKL3000[61]. $BicA^{TM393}$ structure was solved by molecular replacement using Phenix, using the $SLC26Dg^{TM}$ structure as an initial model, and $BicA^{STAS}$ structure was solved by single wavelength anomalous dispersion method. The selenium sites were determined, and initial phases were calculated using the HKL3000[61]. Structure models were refined with Phenix[62] and built manually with Coot[63]. The data collection and refinement statistics are summarized in **Supplementary Table-1**.

SEC-MALS (size exclusion chromatography coupled with multiple angle light scattering). Histidine tagged BicA, $BicA^{TM413}$ and $BicA^{delβ1-2}$ protein were first purified using Ni-affinity chromatography, and further purified using size exclusion chromatography in SEC buffer 20 mM Tris-HCl pH8.0, 100 mM NaCl, 0.018% DDM, and the concentration was around 2 mg/ml. 1 mg/ml BSA was used as the protein standard. The dn/dc (change in refractive index as a function of concentration) value for 0.018% DDM is 0.133, which obtained from previously determined values[64]. 'Protein conjugate' module was used for the molecular mass determination by the

ASTRA method. The data were analyzed with ASTRA software package version 5.3.2.10 (Wyatt Technologies).

Chemical cross-linking experiment. For STAS domain cross-linking experiments, the protein samples were diluted to 0.2 mg/ml in PBS buffer (2 mM KH_2PO_4, 10 mM Na_2HPO_4, 2.7 mM KCl, 137 mM NaCl), then addition of DSS (disuccinimidyl suberate, Pierce) to a final concentration of 5 mM. After a 20 min incubation at 25 °C, the reaction was quenched by addition of 50 mM Tris-HCl (pH8.0, final concentration) for 15 min. The samples were subjected to SDS-PAGE and stained by Coomassie blue. For BicA and $BicA^{TM413}$ cross-linking experiments, the protein samples were diluted to 0.02 mg/ml in PBS buffer, and were incubated with 0 μM, 8 μM, 40 μM and 200 μM DSS at 25 °C for 20 min. The reactions were quenched and the samples were subjected to SDS-PAGE and western blot analysis using the anti-his antibody.

Confocal fluorescence microscopy imaging. Preparation of Syn6803 cells for confocal microscopy imaging was carried out as described earlier [11,59,65,66]. Living cell confocal microscopy imaging was performed on a Zeiss LSM780 inverted confocal microscope with a 100x oil immersion objective (numerical aperture: 1.45) and excitation at 488 nm. Images (12-18 bit, 512 x 512 pixels) were recorded by averaging each scan line eight times. GFP and chlorophyll fluorescence were detected at 500–520 nm and 670–720 nm, respectively. Confocal images were recorded from three different cultures. All images were captured with all pixels below saturation. The inhomogeneity of GFP fluorescence was quantified by taking line profiles of fluorescence intensity around the plasma membranes, smoothing to remove high frequency noise and then computing the standard deviation from the mean fluorescence intensity, which is considered as a key parameter representing the fashion of protein distribution [66].

Cryo-EM and Single-Particle Reconstruction. For cryo-EM sample preparation, purified BicA protein was changed to buffer containing 100 mM NaCl, 20 mM Tris-HCl pH 8.0 and 0.1% digitonin through gel-filtration, and concentrated to ~3 mg/ml. Holey carbon grids (Quantifoil Au R1.2/1.3, 300 mesh) were glow discharged in air for 30 s. 4 μL BicA sample was applied to the grid and incubated in an FEI Vitrobot Mark IV at ~100% relative humidity and 8 °C. Grids were blotted for 3 s and then plunged into liquid ethane cooled by liquid nitrogen. Specimens were imaged with a FEI Tecnai F20 electron microscope operating at 200 kV and equipped with a Gatan K2 Summit direct detector device camera. 759 movies were collected in counting mode with a calibrated pixel size of 1.25 Å. Movies were recorded as 40 frames over 6 s with an exposure rate of ~8 e/pix/s. All images were aligned and averaged using MotionCor2[67] and CTF parameters were estimated using Gctf[68]. After particle picking, manual particle checking and reference-free 2D classification using RELION-2.1[69], 138,124 particles were yielded for further processing. The particle images were used for ab initio structure determination followed by 3D classification, resulting in final density map at around 15.0Å resolution. The crystal structure of $BicA^{TM}$ and $BicA^{STAS}$ were fitted manually into the EM density map using Chimera[70].

Reference

1 Cordat, E. & Casey, J. R. Bicarbonate transport in cell physiology and disease. *Biochem J.* **417**, 423-439, doi:10.1042/BJ20081634 (2009).

2 Miller, A. G., Espie, G. S. & Canvin, D. T. Physiological aspects of CO_2, and HCO_3^- transport by cyanobacteria: a review. *Can. J. Bot.* **68**, 1291-1302 (1990).

3 Murray RB & GD, P. CO_2 concentrating mechanisms in cyanobacteria: molecular components, their diversity and evolution. *J Exp Bot.* **54**, 609-622 (2003).

4 Mackinder, L. C. M. *et al.* A Spatial Interactome Reveals the Protein Organization of the Algal CO_2-Concentrating Mechanism. *Cell* **171**, 133-147 doi:10.1016/j.cell.2017.08.044 (2017).

5 Tatsuo Omata *et al.* Identification of an ATP-binding cassette transporter involved in

bicarbonate uptake in the cyanobacterium *Synechococcus sp*. strain PCC 7942. *Proc Natl Acad Sci U S A.* **96**, 13571–13576 (1999).

6 Shibata, M. *et al.* Genes essential to sodium-dependent bicarbonate transport in cyanobacteria: function and phylogenetic analysis. *J Biol Chem.* **277**, 18658-18664, doi:10.1074/jbc.M112468200 (2002).

7 Price, G. D., Woodger, F. J., Badger, M. R., Howitt, S. M. & Tucker, L. Identification of a SulP-type bicarbonate transporter in marine cyanobacteria. *Proc Natl Acad Sci U S A.* **101**, 18228-18233, doi:10.1073/pnas.0405211101 (2004).

8 Shibata, M. *et al.* Distinct constitutive and low CO2-induced CO2 uptake systems in cyanobacteria: Genes involved and their phylogenetic relationship with homologous genes in other organisms. *Proc Natl Acad Sci U S A.* **98**, 11789-11794, doi:10.1073/pnas.191258298 (2001).

9 Faulkner, M. *et al.* Direct characterization of the native structure and mechanics of cyanobacterial carboxysomes. *Nanoscale* **9**, 10662-10673, doi:10.1039/c7nr02524f (2017).

10 Kerfeld, C. A. & Melnicki, M. R. Assembly, function and evolution of cyanobacterial carboxysomes. *Curr Opin Plant Biol* **31**, 66-75, doi:10.1016/j.pbi.2016.03.009 (2016).

11 Sun, Y. *et al.* Light modulates the biosynthesis and organization of cyanobacterial carbon fixation machinery through photosynthetic electron flow. *Plant Physiol* **171**, 530-541, doi:10.1104/pp.16.00107 (2016).

12 Sun, Y., Wollman, A. J. M., Huang, F., Leake, M. C. & Liu, L. N. Single-Organelle Quantification Reveals Stoichiometric and Structural Variability of Carboxysomes Dependent on the Environment. *The Plant cell* **31**, 1648-1664, doi:10.1105/tpc.18.00787 (2019).

13 Price, G. D. Inorganic carbon transporters of the cyanobacterial CO_2 concentrating mechanism. *Photosynth Res.* **109**, 47-57, doi:10.1007/s11120-010-9608-y (2011).

14 Price GD, Sültemeyer D, Klughammer B, Ludwig M & MR., B. The functioning of the CO_2 concentrating mechanism in several cyanobacterial strains: a review of general physiological characteristics, genes, proteins, and recent advances. *Can. J. Bot.* **76**, 973-1002 (1996).

15 Price, G. D., Badger, M. R., Woodger, F. J. & Long, B. M. Advances in understanding the cyanobacterial CO_2-concentrating-mechanism (CCM): functional components, Ci transporters, diversity, genetic regulation and prospects for engineering into plants. *J Exp Bot.* **59**, 1441-1461, doi:10.1093/jxb/erm112 (2008).

16 McGrath, J. M. & Long, S. P. Can the cyanobacterial carbon-concentrating mechanism increase photosynthesis in crop species? A theoretical analysis. *Plant Physiol* **164**, 2247-2261, doi:10.1104/pp.113.232611 (2014).

17 Rae, B. D. *et al.* Progress and challenges of engineering a biophysical CO_2-concentrating mechanism into higher plants. *J Exp Bot.* **68**, 3717-3737, doi:10.1093/jxb/erx133 (2017).

18 Rolland, V., Badger, M. R. & Price, G. D. Redirecting the cyanobacterial bicarbonate transporters BicA and SbtA to the chloroplast envelope: soluble and membrane cargos need different chloroplast targeting signals in plants. *Front Plant Sci.* **7**, 185, doi:10.3389/fpls.2016.00185 (2016).

19 Uehara, S., Adachi, F., Ito-Inaba, Y. & Inaba, T. Specific and ffficient targeting of cyanobacterial bicarbonate transporters to the inner envelope membrane of chloroplasts in Arabidopsis. *Front Plant Sci.* **7**, 16, doi:10.3389/fpls.2016.00016 (2016).

20 Pengelly, J. J. *et al.* Transplastomic integration of a cyanobacterial bicarbonate transporter

into tobacco chloroplasts. *J Exp Bot.* **65**, 3071-3080, doi:10.1093/jxb/eru156 (2014).

21 Price, G. D. & Howitt, S. M. Topology mapping to characterize cyanobacterial bicarbonate transporters: BicA (SulP/SLC26 family) and SbtA. *Molecular membrane biology* **31**, 177-182, doi:10.3109/09687688.2014.953222 (2014).

22 Shelden, M. C., Howitt, S. M. & Price, G. D. Membrane topology of the cyanobacterial bicarbonate transporter, BicA, a member of the SulP (SLC26A) family. *Mol Membr Biol.* **27**, 12-22, doi:10.3109/09687680903400120 (2010).

23 Alper, S. L. & Sharma, A. K. The SLC26 gene family of anion transporters and channels. *Mol Aspects Med.* **34**, 494-515, doi:10.1016/j.mam.2012.07.009 (2013).

24 Alka, K. & Casey, J. R. Bicarbonate transport in health and disease. *IUBMB life* **66**, 596-615, doi:10.1002/iub.1315 (2014).

25 Nakajima, K., Tanaka, A. & Matsuda, Y. SLC4 family transporters in a marine diatom directly pump bicarbonate from seawater. *Proc Natl Acad Sci U S A.* **110**, 1767-1772, doi:10.1073/pnas.1216234110 (2013).

26 Felce, J. & Saier, M. H., Jr. Carbonic anhydrases fused to anion transporters of the SulP family: evidence for a novel type of bicarbonate transporter. *J Mol Microbiol Biotechnol.* **8**, 169-176, doi:10.1159/000085789 (2004).

27 Igarashi, T. *et al.* Mutations in SLC4A4 cause permanent isolated proximal renal tubular acidosis with ocular abnormalities. *Nat Genet.* **23**, 264-266, doi:10.1038/15440 (1999).

28 Rungroj, N. *et al.* A novel missense mutation in AE1 causing autosomal dominant distal renal tubular acidosis retains normal transport function but is mistargeted in polarized epithelial cells. *J Biol Chem.* **279**, 13833-13838, doi:10.1074/jbc.M400188200 (2004).

29 Kere J, Sistonen P, Holmberg C & A., d. l. C. The gene for congenital chloride diarrhea maps close to but is distinct from the gene for cystic fibrosis transmembrane conductance regulator. *Proc. Natl. Acad. Sci.* **90**, 10686-10689 (1993).

30 Wedenoja, S. *et al.* Update on SLC26A3 mutations in congenital chloride diarrhea. *Hum Mutat.* **32**, 715-722, doi:10.1002/humu.21498 (2011).

31 Everett, L. A. *et al.* Pendred syndrome is caused by mutations in a putative sulphate transporter gene (PDS). *Nat Genet.* **17**, 411-422, doi:Doi 10.1038/Ng1297-411 (1997).

32 Park HJ *et al.* Origins and frequencies of SLC26A4 (PDS) mutations in east and south Asians: global implications for the epidemiology of deafness. *J Med Genet.* **40**, 242–248 (2003).

33 Arakawa T *et al.* Crystal structure of the anion exchanger domain of human erythrocyte band 3. *Science* **350**, 680-684 (2015).

34 Huynh, K. W. *et al.* CryoEM structure of the human SLC4A4 sodium-coupled acid-base transporter NBCe1. *Nat Commun.* **9**, 900, doi:10.1038/s41467-018-03271-3 (2018).

35 Geertsma, E. R. *et al.* Structure of a prokaryotic fumarate transporter reveals the architecture of the SLC26 family. *Nat Struct Mol Biol.* **22**, 803-808, doi:10.1038/nsmb.3091 (2015).

36 Alguel, Y. *et al.* Structure of eukaryotic purine/H(+) symporter UapA suggests a role for homodimerization in transport activity. *Nat Commun.* **7**, 11336, doi:10.1038/ncomms11336 (2016).

37 Xu, M. *et al.* Properties of mutants of *Synechocystis sp*. strain PCC 6803 lacking inorganic carbon sequestration systems. *Plant Cell Physiol.* **49**, 1672-1677, doi:10.1093/pcp/pcn139 (2008).

38 Thurtle-Schmidt, B. H. & Stroud, R. M. Structure of Bor1 supports an elevator transport

mechanism for SLC4 anion exchangers. *Proc Natl Acad Sci U S A.* **113**, 10542-10546, doi:10.1073/pnas.1612603113 (2016).

39 Lu, F. *et al.* Structure and mechanism of the uracil transporter UraA. *Nature* **472**, 243-246, doi:10.1038/nature09885 (2011).

40 Yu, X. *et al.* Dimeric structure of the uracil:proton symporter UraA provides mechanistic insights into the SLC4/23/26 transporters. *Cell Res.* **27**, 1020-1033, doi:10.1038/cr.2017.83 (2017).

41 Yamashita, A., Singh, S. K., Kawate, T., Jin, Y. & Gouaux, E. Crystal structure of a bacterial homologue of Na^+/Cl^--dependent neurotransmitter transporters. *Nature* **437**, 215-223, doi:10.1038/nature03978 (2005).

42 Mancusso, R., Gregorio, G. G., Liu, Q. & Wang, D. N. Structure and mechanism of a bacterial sodium-dependent dicarboxylate transporter. *Nature* **491**, 622-626, doi:10.1038/nature11542 (2012).

43 Jennings, M. L. & Smith, J. S. Anion-proton cotransport through the human red blood cell band 3 protein. Role of glutamate 681. . *J. Biol. Chem.* **267**, 13964–13971 (1992).

44 Detro-Dassen S *et al.* Conserved dimeric subunit stoichiometry of SLC26 multifunctional anion exchangers. *J Biol Chem.* **283**, 4177-4188, doi:10.1074/jbc.M704924200 (2008).

45 Greeson, J. N., Organ, L. E., Pereira, F. A. & Raphael, R. M. Assessment of prestin self-association using fluorescence resonance energy transfer. *Brain Res.* **1091**, 140-150, doi:10.1016/j.brainres.2006.02.084 (2006).

46 Compton, E. L., Karinou, E., Naismith, J. H., Gabel, F. & Javelle, A. Low resolution structure of a bacterial SLC26 transporter reveals dimeric stoichiometry and mobile intracellular domains. *J Biol Chem.* **286**, 27058-27067, doi:10.1074/jbc.M111.244533 (2011).

47 Srinivasan, L., Baars, T. L., Fendler, K. & Michel, H. Functional characterization of solute carrier (SLC) 26/sulfate permease (SulP) proteins in membrane mimetic systems. *Biochim Biophys Acta.* **1858**, 698-705, doi:10.1016/j.bbamem.2016.01.006 (2016).

48 Gorbunov, D. *et al.* Molecular architecture and the structural basis for anion interaction in prestin and SLC26 transporters. *Nature communications* **5**, 3622, doi:10.1038/ncomms4622 (2014).

49 Dorwart, M. R. *et al.* Congenital chloride-losing diarrhea causing mutations in the STAS domain result in misfolding and mistrafficking of SLC26A3. *J Biol Chem.* **283**, 8711-8722, doi:10.1074/jbc.M704328200 (2008).

50 Dossena S *et al.* Molecular and functional characterization of human pendrin and its allelic variants. *Cell Physiol Biochem.* **28**, 451-466 (2011).

51 Drew, D. & Boudker, O. Shared molecular mechanisms of membrane transporters. *Annu Rev Biochem.* **85**, 543-572, doi:10.1146/annurev-biochem-060815-014520 (2016).

52 Compton, E. L. *et al.* Conserved structure and domain organization among bacterial SLC26 transporters. *The Biochemical journal* **463**, 297-307, doi:10.1042/BJ20130619 (2014).

53 Walter, J. D., Sawicka, M. & Dutzler, R. Cryo-EM structures and functional characterization of murine Slc26a9 reveal mechanism of uncoupled chloride transport. *Elife* **8**, doi:10.7554/eLife.46986 (2019).

54 Ko, S. B. *et al.* Gating of CFTR by the STAS domain of SLC26 transporters. *Nat Cell Biol.* **6**, 343-350, doi:10.1038/ncb1115 (2004).

55 Shibagaki, N. & Grossman, A. R. Binding of cysteine synthase to the STAS domain of sulfate

transporter and its regulatory consequences. *J Biol Chem.* **285**, 25094-25102, doi:10.1074/jbc.M110.126888 (2010).

56 Fang, Y. *et al.* Engineering and modulating functional cyanobacterial CO_2-fixing organelles. *Frontiers in plant science* **9**, 739, doi:10.3389/fpls.2018.00739 (2018).

57 Lin, M. T., Occhialini, A., Andralojc, P. J., Parry, M. A. & Hanson, M. R. A faster Rubisco with potential to increase photosynthesis in crops. *Nature* **513**, 547-550, doi:10.1038/nature13776 (2014).

58 Long, B. M. *et al.* Carboxysome encapsulation of the CO_2-fixing enzyme Rubisco in tobacco chloroplasts. *Nature communications* **9**, 3570, doi:10.1038/s41467-018-06044-0 (2018).

59 Casella, S. *et al.* Dissecting the Native Architecture and Dynamics of Cyanobacterial Photosynthetic Machinery. *Mol Plant* **10**, 1434-1448, doi:10.1016/j.molp.2017.09.019 (2017).

60 Bao, Z. *et al.* Structure and mechanism of a group-I cobalt energy coupling factor transporter. *Cell Res.* **27**, 675-687, doi:10.1038/cr.2017.38 (2017).

61 Minor, W., Cymborowski, M., Otwinowski, Z. & Chruszcz, M. HKL-3000: the integration of data reduction and structure solution-from diffraction images to an initial model in minutes. *Acta Crystallogr D Biol Crystallogr.* **62**, 859-866, doi:10.1107/S0907444906019949 (2006).

62 Adams, P. D. *et al.* PHENIX: a comprehensive Python-based system for macromolecular structure solution. *Acta Crystallogr D Biol Crystallogr.* **66**, 213-221, doi:10.1107/S0907444909052925 (2010).

63 Emsley P & K, C. Coot: Model-building tools for molecular graphics. *Acta Crystallogr D Biol Crystallogr.* **60**, 2126–2132 (2004).

64 Slotboom, D. J., Duurkens, R. H., Olieman, K. & Erkens, G. B. Static light scattering to characterize membrane proteins in detergent solution. *Methods* **46**, 73-82, doi:10.1016/j.ymeth.2008.06.012 (2008).

65 Huang, F. *et al.* Roles of RbcX in carboxysome biosynthesis in the Cyanobacterium *Synechococcus elongatus* PCC7942. *Plant Physiol* **179**, 184-194, doi:10.1104/pp.18.01217 (2019).

66 Liu, L. N. *et al.* Control of electron transport routes through redox-regulated redistribution of respiratory complexes. *Proc Natl Acad Sci U S A.* **109**, 11431-11436, doi:10.1073/pnas.1120960109 (2012).

67 Zheng, S. Q. *et al.* MotionCor2: anisotropic correction of beam-induced motion for improved cryo-electron microscopy. *Nature methods* **14**, 331-332, doi:10.1038/nmeth.4193 (2017).

68 Zhang, K. Gctf: Real-time CTF determination and correction. *J Struct Biol* **193**, 1-12, doi:10.1016/j.jsb.2015.11.003 (2016).

69 Scheres, S. H. RELION: implementation of a Bayesian approach to cryo-EM structure determination. *J Struct Biol* **180**, 519-530, doi:10.1016/j.jsb.2012.09.006 (2012).

70 Pettersen, E. F. *et al.* UCSF Chimera--a visualization system for exploratory research and analysis. *J Comput Chem* **25**, 1605-1612, doi:10.1002/jcc.20084 (2004).

Correspondence and requests for materials should be addressed to Peng Zhang: pengzhang01@sibs.ac.cn

Acknowledgements

We thank the staff members at BL19U1/BL17U1-SSRF and National Protein Science Center (Shanghai) for technical assistance in Diffraction data and SEC-MALS data collection, and staff members at the Cryo-EM center of University of Science and Technology of China and National Protein Science Center (Shanghai) for Cryo-EM analysis and data collection. We also thank the staff members at the core facility center of Institute of Plant Physiology and Ecology for X-ray diffraction analysis.

This work was supported by grants from the National Natural Science Foundation of China (31861130356 to P.Z.), the Ministry of Science and Technology of China (2015CB910900 to P.Z.), the Chinese Academy of Sciences (XDB27020103 and QYZDB-SSW-SMC006 to P.Z.); and the grants from the Royal Society (NAF\R1\180433 to P.Z., and UF120411 and URF\R\180030 to L.L.), the Biotechnology and Biological Sciences Research Council (BB/M024202/1 and BB/R003890/1 to L.L.), an award from the University of Liverpool Technology Directorate Voucher Scheme (to F.H.), and the Leverhulme Trust Early Career Fellowship (ECF-2016-778 to F.H.). The atomic coordinates and structure factors for the structures have been deposited in the Protein Data Bank with accession codes **6KI1** and **6KI2**. The Cryo-EM map of BicA has been deposited in the EMDB (EMD-9897).

Author Contributions

P.Z. conceived the project. C.W. and P.Z. designed the experiments. C.W. performed the majority of the experiments; B.S. contributed to the LCP crystallization; X.Z. and X.H. carried out the Cryo-EM study; H.G. and F.Y. contributed to protein expression and crystallization; M.Z. contributed to transport assay analysis; X.C., and H.M. contributed to growth assay analysis; F.H., T.C. and L.L. carried out genetic GFP fusion and living cell imaging. P.Z. and C.W. solved the crystal structures. P.Z., L.L. and C.W. wrote the manuscript with inputs from all authors.

Competing interests

The authors declare no competing interests.

Figure legends

Fig. 1. Functional characterization of BicA. **a**, Growth curves of *Synechocystis sp.* PCC6803 WT and Δ4/Δ5 mutant cells under condition bubbled with air. **b**, Growth of WT and Δ4/Δ5 mutants cells bubbled with air. The photo was taken after 72 hours of growth (experiments were repeated three times). **c**, The construction design of the Δ5 rescue strain. **d**, Growth curves of Δ4, Δ5, and Δ5 complemented with BicA or $BicA^{TM413}$. (Values are mean ± SD/standard deviations, n=3)

Fig. 2. The overall structure of $BicA^{TM}$. a, Cylinder cartoon shows the side view of the $BicA^{TM}$ core domain (orange) and gate domain (blue). The transmembrane helices are numbered and the substrate-HCO_3^- are shown with a ball-and-stick model. **b**, Topology of $BicA^{TM}$. **c**, A bottom view shows the core domain/gate domain and the bound monoolein (magenta sticks) and HCO_3^-.

Fig. 3. Substrate binding site of BicA. a, Electron static surface shows the HCO_3^- and metal ion binding site in the core domain. Negative and positive charges are shown respectively in red and blue color, HCO_3^- is show with a ball-and-stick model and metal ion is show with a purple sphere. **b**, Zoom-in view of the substrate-binding site shows the coordinates. Coordinating residues are shown with sticks and transmembrane helices are colored in orange. **c**, Growth curves of Δ5, Δ5 complemented with BicA, and mutants with substrate-binding site mutations. (Values are mean ± SD, n=3)

Fig. 4. Structural comparison of the substrate-binding sites. a, Comparison of TM3 and TM10 of SLC26/23 family transporters BicA, UapA (PDB: 5I6C, colored in dark gray) and UraA (PDB: 3QE7, colored in gray). **b**, Comparison of TM3 and TM10 of bicarbonate transporters BicA, AE1 (PDB: 4YZF, colored in blue) and NBCe1 (PDB: 6CAA, colored in light blue). **c**, Comparison of the substrate-binding site residues of BicA, AE1 (PDB: 4YZF) and NBCe1 (PDB: 6CAA). **d**, Sequence alignment of residues constituting the substrate-binding site in different bicarbonate transporters. The alignment includes three human SLC4 family Cl^-/HCO_3^- antiporters: SLC4A1 (GI 4507021), SLC4A2 (GI 20306918), and SLC4A3 (GI 157671951); four human SLC4 family Na^+/HCO_3^- symporters: SLC4A4 (GI 74721543), SLC4A5 (GI 182691595), SLC4A7 (GI 229462789) and SLC4A9 (GI 29427950)); four human SLC26 family Cl^-/HCO_3^- antiporters: SLC26A3 (GI 19343676), SLC26A4 (GI 119603820) and SLC26A6 (GI 94721253); *Synechocystis sp*. PCC6803 Na^+/HCO_3^- transporter BicA (GI 499176153).

Fig. 5. $BicA^{STAS}$ is required for BicA dimer formation. a, Overall structure of $BicA^{STAS}$ dimer, two protomers are colored in cyan and gray respectively (top view). **b**, Side view of $BicA^{STAS}$ dimer. **c-e**, SEC-MALS results of BicA, $BicA^{TM413}$ and STAS domain β1-β2 deletion mutant ($BicA^{del\beta1\text{-}2}$). The red, blue and green lines represent the molecular weight (Mw) of protein, detergent micelle and protein-detergent complex, respectively. The curves of light scattering and UV absorbance are shown with solid and dotted lines, respectively, experiments were repeated three times with similar results.

Fig. 6. BicA dimer structure and physiological significance. a, Envelope structure of BicA obtained using Cryo-EM (front view). $BicA^{TM}$ and $BicA^{STAS}$ crystal structures were fitted to the envelope (colored gray and slate blue). **b**, Bottom view of BicA structure showing the $BicA^{STAS}$ dimer. **c**, Human disease mutations identified in SLC26 family bicarbonate transporters were plotted on the dimer interface of $BicA^{STAS}$. **d**, Growth curves of Δ5 strains complemented with BicA or BicA mutations at the $BicA^{STAS}$ dimer interface (values are mean ± SD, n=3). **e**, Living-cell confocal images revealing the relative even distribution of BicA-GFP and the spotty distribution of $BicA^{TM413}$-GFP (arrows) in the plasma membranes of Syn6803. Chlorophyll fluorescence is shown in red and GFP fluorescence is shown in green (confocal images were recorded from three different cultures). **f**, fluorescence profile deviation analysis confirming the different distribution patterns (*** p =0.0008, two tailed Student's t-test) of BicA-GFP (13.82 ± 0.29, n = 30) and $BicA^{TM413}$-GFP (17.62 ± 0.40, n = 30). Error bars represent standard error of mean (SEM).

Fig. 7. Transport mechanism of Na^+ dependent HCO_3^- transporters BicA and NBCe1. a, Inward-facing and outward-facing conformations represented by $BicA^{TM}$ and $NBCe1^{CTD}$. The orientations of BicA and NBCe1 are aligned through the gate domain. $BicA^{TM}$ and $NBCe1^{CTD}$ are shown with surface models and the substrate-binding site of NBCe1 is denoted with a red star. **b**, Zoom-in view shows the core domain movement of BicA (orange) and NBCe1 (light blue). **c**, Elevator mechanism of BicA and NBCe1. The core domain and gate domain are shown with bright-orange and light-blue colored cartoon. HCO_3^- and Na^+ are shown with red stars and blue spheres, respectively.

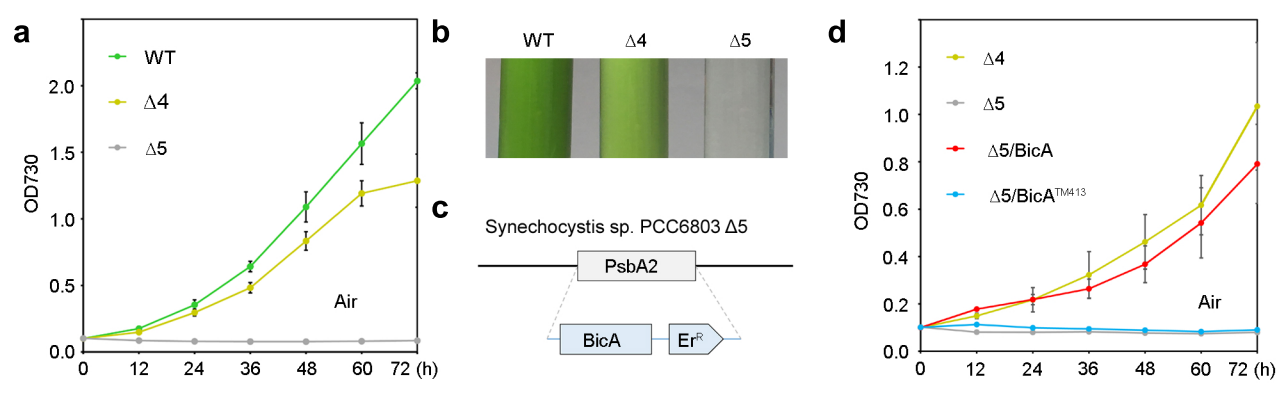
a
WT
Δ4
Δ5
OD730
2.0
1.5
1.0
0.5
0.0
Air
0
12
24
36
48
60
72 (h)
b
WT
Δ4
Δ5
c
Synechocystis sp. PCC6803 Δ5
PsbA2
BicA
Er^R
d
Δ4
Δ5
Δ5/BicA
Δ5/BicA^TM413
OD730
1.2
1.0
0.8
0.6
0.4
0.2
0.0
Air
0
12
24
36
48
60
72 (h)

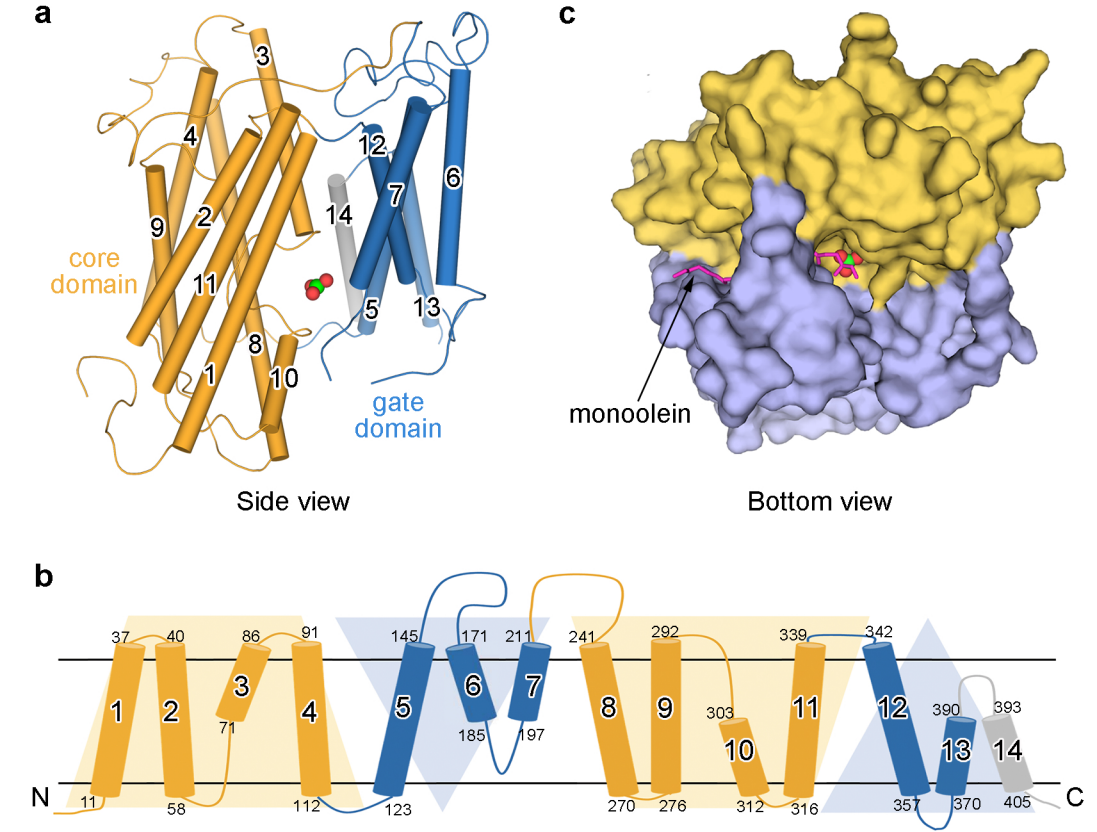
a
3
4
12
6
7
14
9
2
core
domain
11
5
13
8
1
10
gate
domain
Side view
c
monoolein
Bottom view
b
37
40
86
91
145
171
211
241
292
339
342
1
2
3
4
5
6
7
8
9
10
11
12
71
185
197
303
390
393
13
14
N
11
58
112
123
270
276
312
316
357
370
405
C

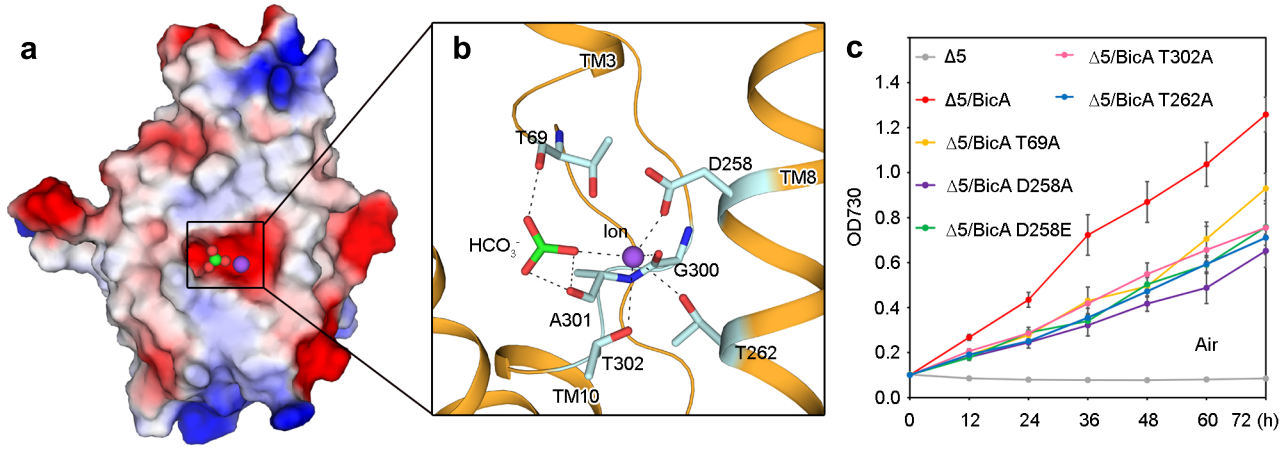
a
b
TM3
T69
D258
TM8
HCO3-
Ion
G300
A301
T302
T262
TM10
c
Δ5
Δ5/BicA
Δ5/BicA T69A
Δ5/BicA D258A
Δ5/BicA D258E
Δ5/BicA T302A
Δ5/BicA T262A
Air
OD730
0.0
0.2
0.4
0.6
0.8
1.0
1.2
1.4
0
12
24
36
48
60
72 (h)

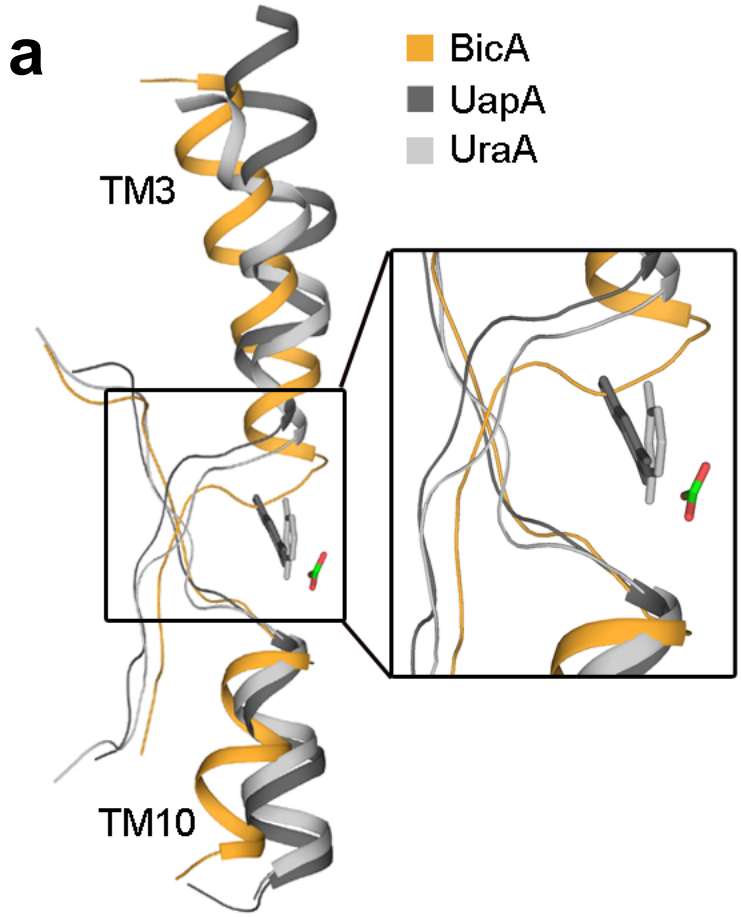

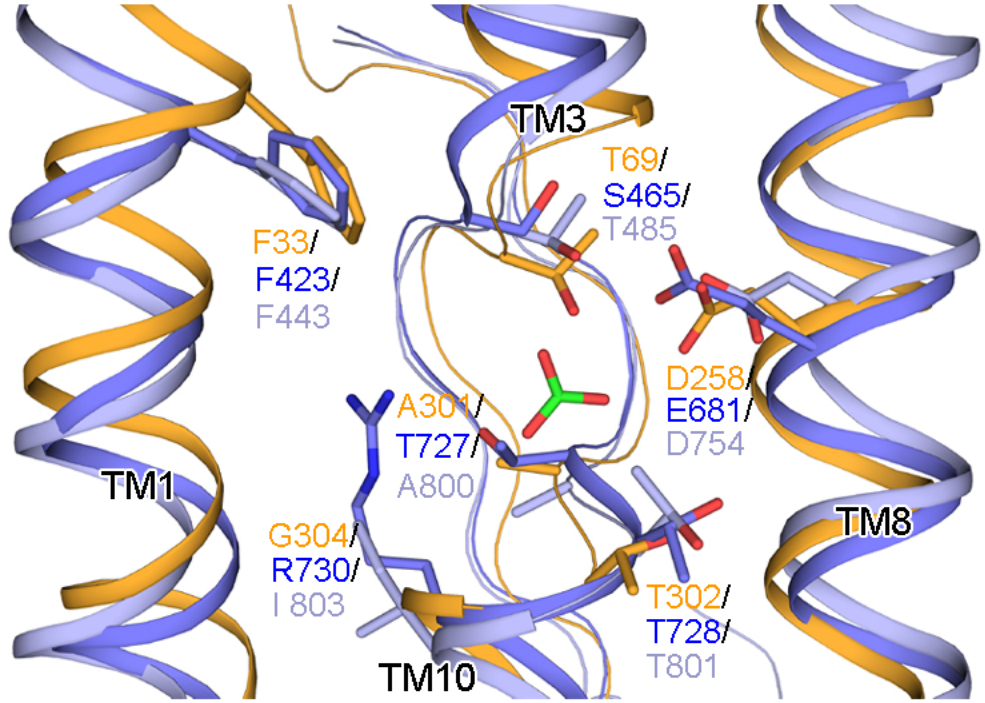

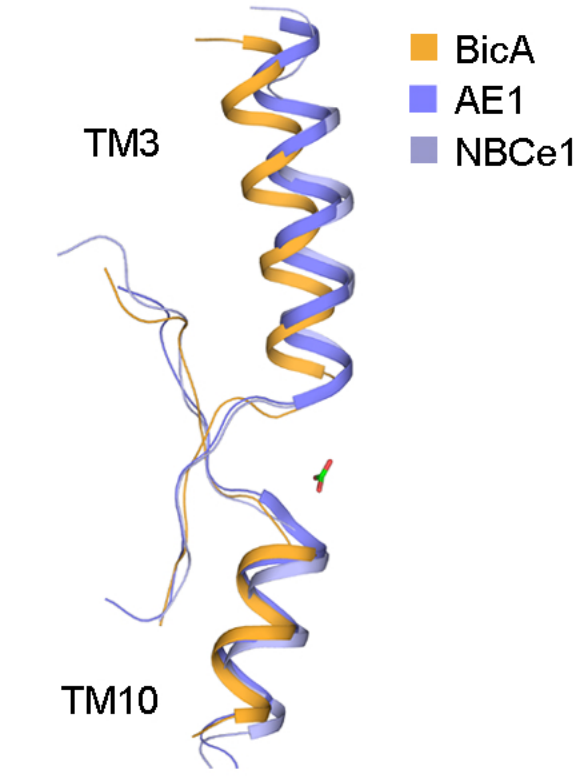

d

	TM3	TM8	TM10	Coupled Ions
hSLC4A1(AE1)	F S G	E S Q I T	T T V R	Cl^-
hSLC4A2	F S G	E T Q I T	A T V R	Cl^-
hSLC4A3	F S G	E T Q I T	A T V R	Cl^-
hSLC4A4(NBCe1)	S T G	D Q Q I T	A T V I	Na^+
hSLC4A5	S T G	D Q Q I T	A T V I	Na^+
hSLC4A7	S T G	D Q Q I T	A T V I	Na^+
hSLC4A9	S T G	D Q Q I T	A T V I	Na^+
hSLC26A3	P F P	V A F S V	A L S R	Cl^-
hSLC26A4	P F P	I A V S V	A L S R	Cl^-
hSLC26A6	T F A	I A A L A	S M S R	Cl^-
BicA(SLC26)	P T G	D A L L T	A T M G	Na^+
	69	258 262	301/302 304	

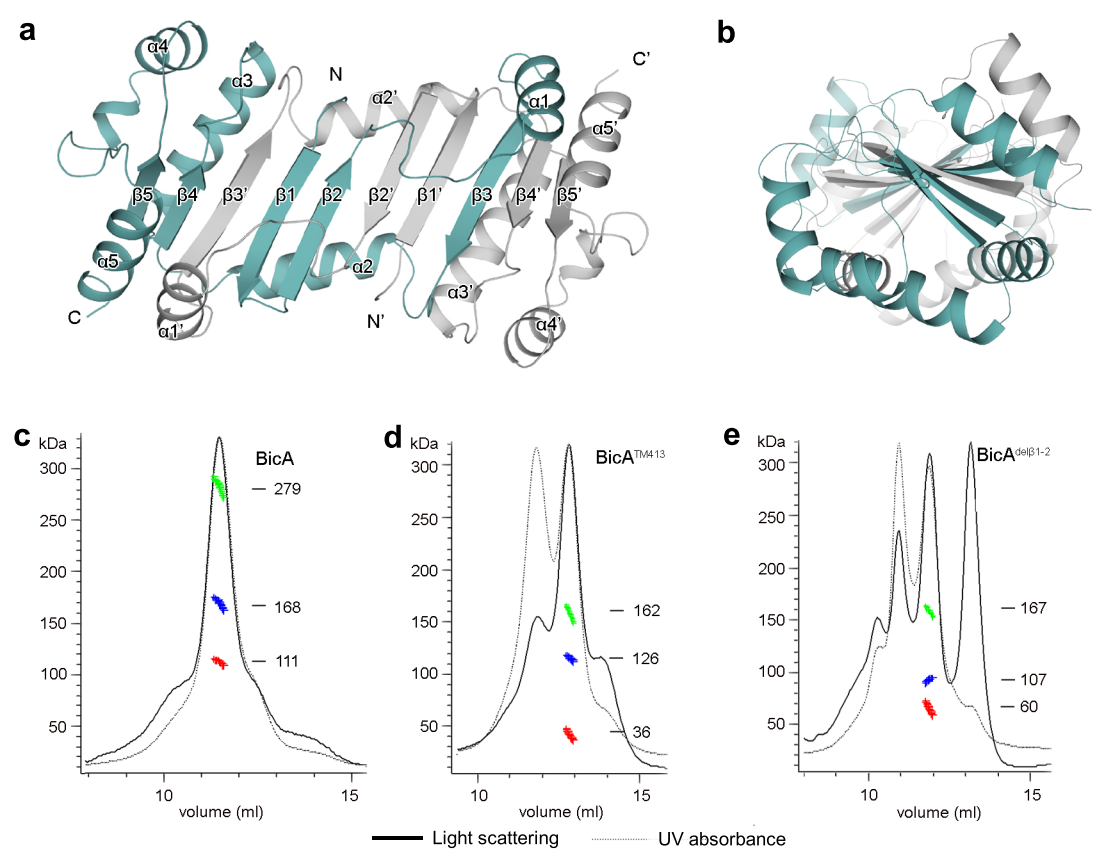
a
α4
α3
N
α2'
α1
C'
α5'
β5
β4
β3'
β1
β2
β2'
β1'
β3
β4'
β5'
α5
α2
α3'
C
α1'
N'
α4'
b
c
kDa
BicA
279
168
111
volume (ml)
d
kDa
BicA TM413
162
126
36
volume (ml)
e
kDa
BicA delβ1-2
167
107
60
volume (ml)
Light scattering
UV absorbance

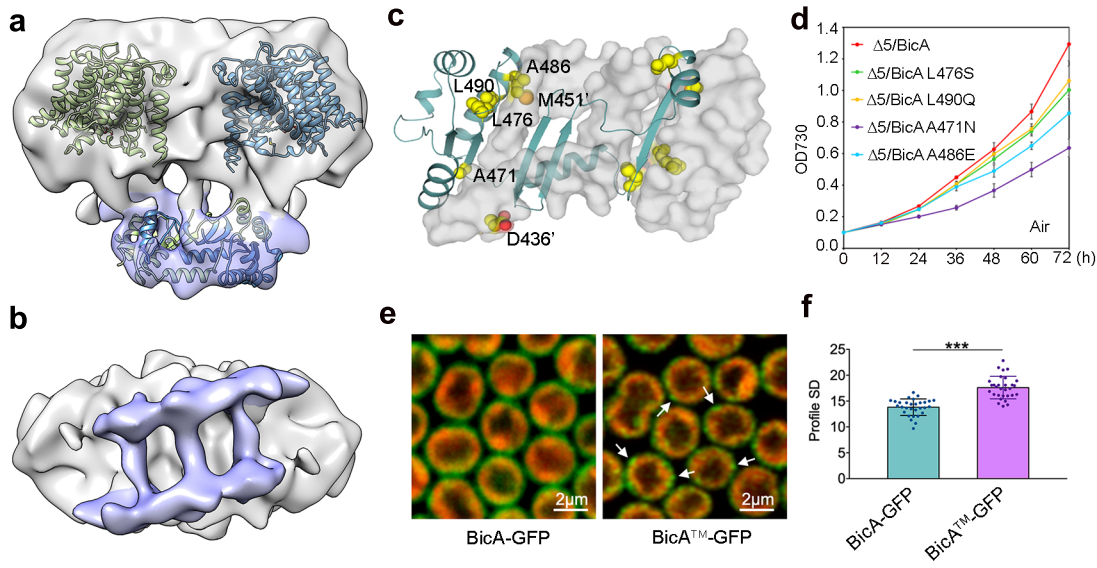
a
b
c
A486
L490
M451'
L476
A471
D436'
d
Δ5/BicA
Δ5/BicA L476S
Δ5/BicA L490Q
Δ5/BicA A471N
Δ5/BicA A486E
OD730
Air
0
12
24
36
48
60
72
(h)
e
2μm
2μm
BicA-GFP
BicA™-GFP
f
***
Profile SD
BicA-GFP
BicA™-GFP

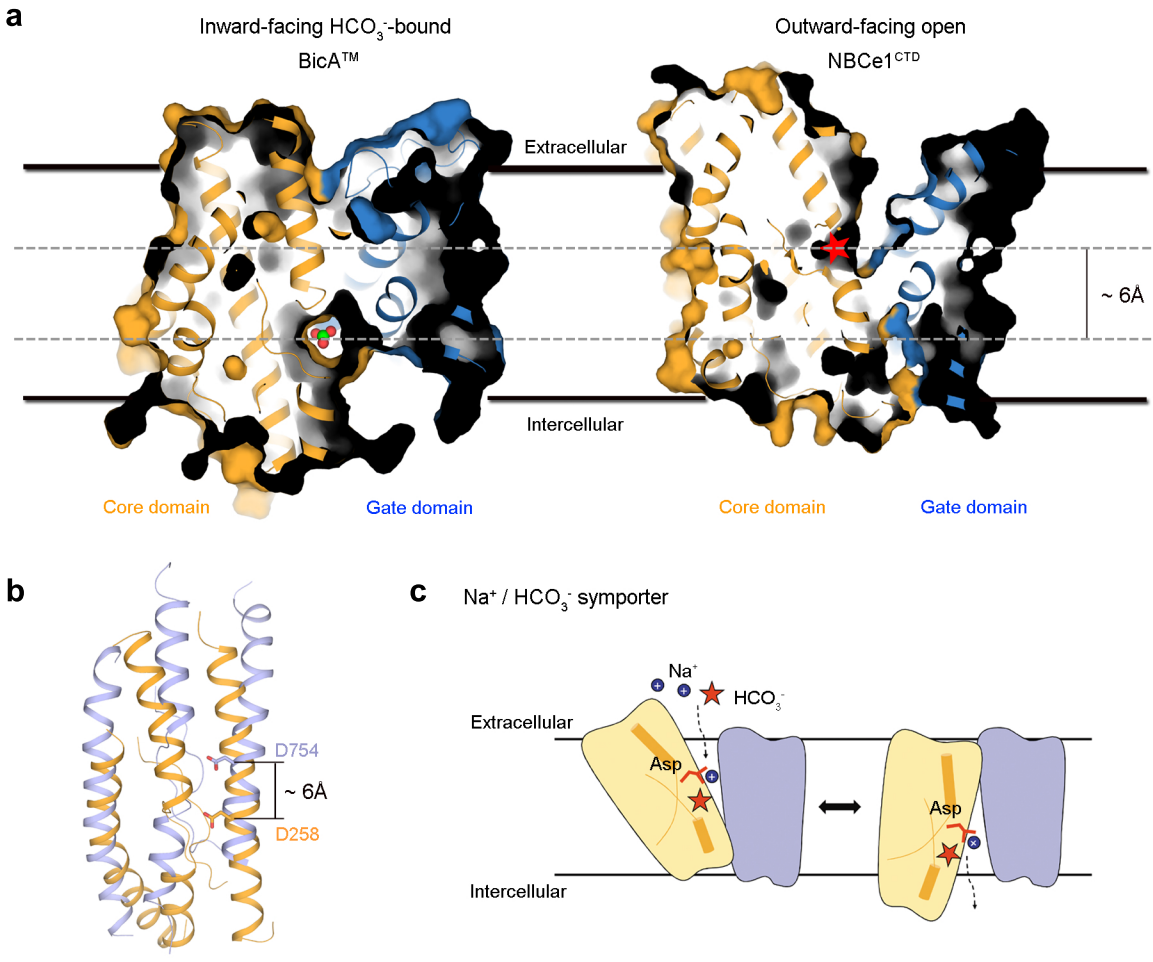
a
Inward-facing HCO_3^--bound
BicA^{TM}
Outward-facing open
NBCe1^{CTD}
Extracellular
Intercellular
~ 6Å
Core domain
Gate domain
Core domain
Gate domain
b
D754
~ 6Å
D258
c
Na^+ / HCO_3^- symporter
Na^+
HCO_3^-
Extracellular
Asp
Asp
Intercellular